A&A 632, L5 (2019)
https://doi.org/10.1051/0004-6361/201936760

Astronomy & Astrophysics

LETTER TO THE EDITOR

The Hayabusa2 lander MASCOT on the surface of asteroid (162173) Ryugu – Stereo-photogrammetric analysis of MASCam image data

F. Scholten[1], F. Preusker[1], S. Elgner[1], K.-D. Matz[1], R. Jaumann[1], M. Hamm[1], S. E. Schröder[1], A. Koncz[1], N. Schmitz[1], F. Trauthan[1], M. Grott[1], J. Biele[2], T.-M. Ho[3], S. Kameda[4], and S. Sugita[5,6]

[1] German Aerospace Center (DLR), Institute of Planetary Research, 12489 Berlin, Germany
e-mail: Frank.Scholten@dlr.de
[2] German Aerospace Center (DLR), Microgravity User Support Center (MUSC), Cologne, Germany
[3] German Aerospace Center (DLR), Institute of Space Systems, Bremen, Germany
[4] Department of Physics, Rikkyo University, 3-34-1 Nishi-Ikebukuro, Toshima, Tokyo, Japan
[5] University of Tokyo, 7-3-1 Hongo, Bunkyo, Tokyo, Japan
[6] Planetary Exploration Research Center, Chiba Institute of Technology, 2-17-1 Tsudanuma, Narashino, Chiba, Japan

Received 23 September 2019 / Accepted 7 November 2019

ABSTRACT

After its release and a descent and bouncing phase, the Hayabusa2 lander MASCOT came to a final rest and MASCOT's camera MASCam acquired a set of images of the surface of Ryugu. With MASCam's instantaneous field of view of about 1 mrad, the images provide pixel scales from 0.2 to 0.5 mm pixel^{-1} in the foreground and up to 1 cm pixel^{-1} for surface parts in the background. Using a stereo-photogrammetric analysis of the MASCam images taken from slightly different positions due to commanded and unintentional movements of the MASCOT lander, we were able to determine the orientation for the different measurement positions. Furthermore, we derived a 3D surface model of MASCOT's vicinity. Although the conditions for 3D stereo processing were poor due to very small stereo angles, the derived 3D model has about 0.5 cm accuracy in the foreground at 20 cm distance and about 1.5 cm at a distance of 40–50 cm.

Key words. minor planets, asteroids: general – minor planets, asteroids: individual: (162173) Ryugu – planets and satellites: surfaces

1. Introduction

The spacecraft of the Japanese Hayabusa2 (HY2) mission (Watanabe et al. 2017) reached its target asteroid (162173) Ryugu in 2018 (Watanabe et al. 2019). On 3 October 2018, the German-French MASCOT lander (Mobile Asteroid surface SCOuT, Ho et al. 2017) was released from low altitude. MASCOT's descent and bouncing path until its first settlement point (SP1) has been reconstructed (Scholten et al. 2019) from data of the Optical Navigation Camera system (ONC; Kameda et al. 2017; Sugita et al. 2019) onboard the HY2 spacecraft and from measurements of several instruments onboard MASCOT itself (MASCam, MARA, MASMag). MASCOT's camera MASCam (Jaumann et al. 2017, 2019) acquired images during its descent phase, within its bouncing phase, and after coming to rest on the surface of Ryugu. After an uprighting procedure and a first relocation, MASCam acquired images of its close vicinity from slightly different positions over a time span of about 10 h until MASCOT's operational end after a total operation time of about 17 h. For the majority of subsequent scientific analyses, including those from other instruments onboard MASCOT, such as for example the MASCOT radiometer MARA (Grott et al. 2016, 2019), and for the full exploitation of the acquired image data, it is a requirement to reference the different images geometrically, relative to each other, as well as absolutely, with respect to body-fixed coordinates. This provides relevant characteristics (e.g., image orientation, scale, geolocation, 3D surface models, and accurate information about observation and illumination conditions) for the entire image content. A comprehensive tool for the derivation of this kind of information is a set of general and mission-specific stereo-photogrammetric (SPG) techniques developed at the German Aerospace Center (DLR) and successfully applied to a variety of image datasets from different space missions to planets, satellites, asteroids, and comets during the past 20 years (e.g., Gwinner et al. 2009, 2010; Scholten et al. 2012; Preusker et al. 2011, 2012, 2017, 2019). Within this Letter, we describe how we integrated context results for MASCOT (Preusker et al. 2019) and descent and bouncing path information (Scholten et al. 2019) to derive a precise description of the orientation of MASCam/MASCOT for the different measurement positions during on-ground operations. Finally, we derived a local 3D surface model of the vicinity of MASCOT's on-ground resting positions.

2. Relevant input information

2.1. Commanded movements of MASCOT

Scholten et al. (2019) describes MASCOT's arrival at the first settlement point (SP1) on 2018-10-03 at 02:14:17 UTC at 22.2065° south, 317.2991° east, 446.25 m radius, resting on MASCOT's +y-side (see Sect. 2.4). For the execution of intentional movements (uprighting, relocation, and mini-move) on ground, MASCOT is equipped with a mobility mechanism

(Ho et al. 2017). After a first use of this mechanism within an uprighting procedure, MASCOT came to rest on the first measurement point (MP1) on the surface of Ryugu at 02:34:19 (Jaumann et al. 2019). Instrument data from the first science cycle showed that MASCOT was in an upside-down position (MASCam images from MP1 show mostly sky). Therefore, a relocation was commanded, which left MASCOT at 08:27:51 in a correct orientation for a second science cycle at its second measurement point (MP2). After a mini-move, performed at 16:30:41, MASCOT reached its third measurement point (MP3) for a third science cycle. With an additional relocation at 18:05:41, MASCOT's fourth science cycle started at its fourth measurement point (MP4). However, the only MASCam image from MP4 shows that MASCOT was in a non-upright position. Finally, the nominal MASCOT operation ended shortly after 19:04 (Jaumann et al. 2019).

2.2. Unintentional movements of MASCOT

Apart from the commanded movements (MP1→MP2, MP2→MP3, and MP3→MP4), parallaxes of identical surface features within MASCam images from different sequences at MP2 and MP3 indicate additional unintentional smaller slides at MP1-3. While the first MASCam images from MP1 show only sky, faint surface structures are visible at the edge of the last images at MP1. Some unintentional sliding or change of orientation must have happened between 06:33:38 and 07:32:43. Therefore, we defined two measurement positions for MP1 (MP1a and MP1b). Two unintentional slides occurred at MP2, a first slide between 08:30:54 and 10:52:21 and a second slide between 10:53:22 and 11:54:08. These slides split MP2 into three slightly different measurement points (MP2a, MP2b, and MP2c). Finally, one unintentional slide occurred at MP3 between 16:40:18 and 17:17:48 and split MP3 into two different measurement points (MP3a and MP3b).

2.3. MASCOT as seen in ONC images

There are ONC images that show MASCOT during its science operation on ground. On Oct. 3, three ONT-T images show MASCOT on MP3b between 17:15:10 and 17:31:50. Based on a surface model and orthoimage maps (Preusker et al. 2019), we determined the Ryugu body-fixed frame (RBFF) coordinates of MP3b, that is, 22.3068° south, 317.1527° east, 446.25 m radius. Thus, the total movement from SP1 to MP3 was about 1.3 m. On the next day, an additional set of four ONC-T images acquired between 00:21:59 and 00:55:09 shows MASCOT on MP4 at 22.2940° south, 317.1610° east, 446.16 m radius. This indicates that the movement by the last relocation from MP3b to MP4 was as small as 0.12 m.

2.4. The MASCOT coordinate frame

All previously presented RBFF coordinates for MASCOT positions (SP1, MP3b, MP4) are the RBFF coordinates of the geometric center of the MASCOT lander. In the following, we provide coordinates that define RBFF positions of the origin of the MASCOT body-fixed frame (MBFF), which is located on the bottom plate of MASCOT. Figure 1 displays MASCOT and its dimensions, the origin of the MBFF coordinate frame, and the positions of the relevant MASCOT structures for this investigation (MASCam and MARA). Figure 1 also shows an alignment cube from MASCOT's assembly (Jaumann et al. 2019), which is of importance later on within our analysis. The deviations

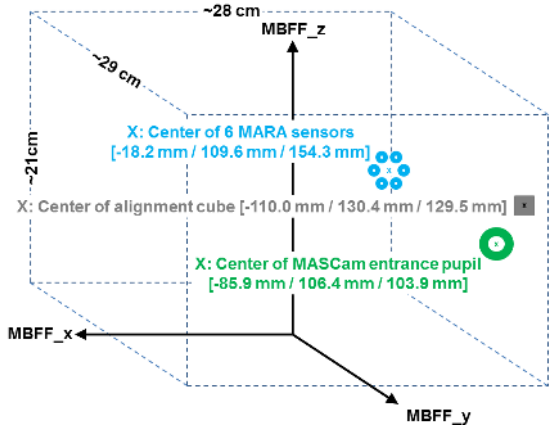

Fig. 1. Relevant structures in the MASCOT body-fixed frame.

Table 1. Initial RBFF coordinates of the MBFF origin (partly updated later on, see Sect. 4 and Table 3).

Position	Latitude [° South]	Longitude [° East]	Radius [m]
SP1	22.2065	317.2991	446.25
MP3b	22.3068	317.1527	446.15
MP4	22.2949	317.1610	446.37

Notes. The uncertainty of the parameters in absolute sense are about ±10 cm.

of the boresight vectors to the MBFF_y-direction for MASCam (22° towards MBFF_$-z$) and MARA (40° towards MBFF_$-z$, 4° to the MBFF_$-x$) are defined in a SPICE frame kernel (Acton 1996). If we consider MASCOT's respective orientation at SP1, MP3b, and MP4 (resting on the MBFF +y-side, nominal, and upside-down), RBFF coordinates of the respective MBFF origin are listed in Table 1.

2.5. MASCam on-ground images

In total, MASCam acquired about 100 images during its four science cycles on the surface of Ryugu. Apart from images taken without artificial illumination, an array of light-emitting diodes (LEDs) in four different colors was used during night and daytime. Figure 2 shows typical MASCam images acquired with the red LED, which we used in our analysis. The known local times and the Sun direction within these images indicate that the viewing directions are close to north.

3. MASCOT's measurement positions and attitudes on the surface of Ryugu

The position and attitude of MP3b and MP4 are already at least partly determined. However, the others measurement positions require a more detailed analysis. In this section, we describe our analysis towards preliminary orientations, which are refined below in Sect. 4.

3.1. Measurement position MP1

MASCOT's position and attitude at MP1a and MP1b are not constrained directly by images from the ONC. MASCam images indicate that the orientation during the first science cycle at MP1 was generally upside-down. Visibilities of Jupiter, Saturn,

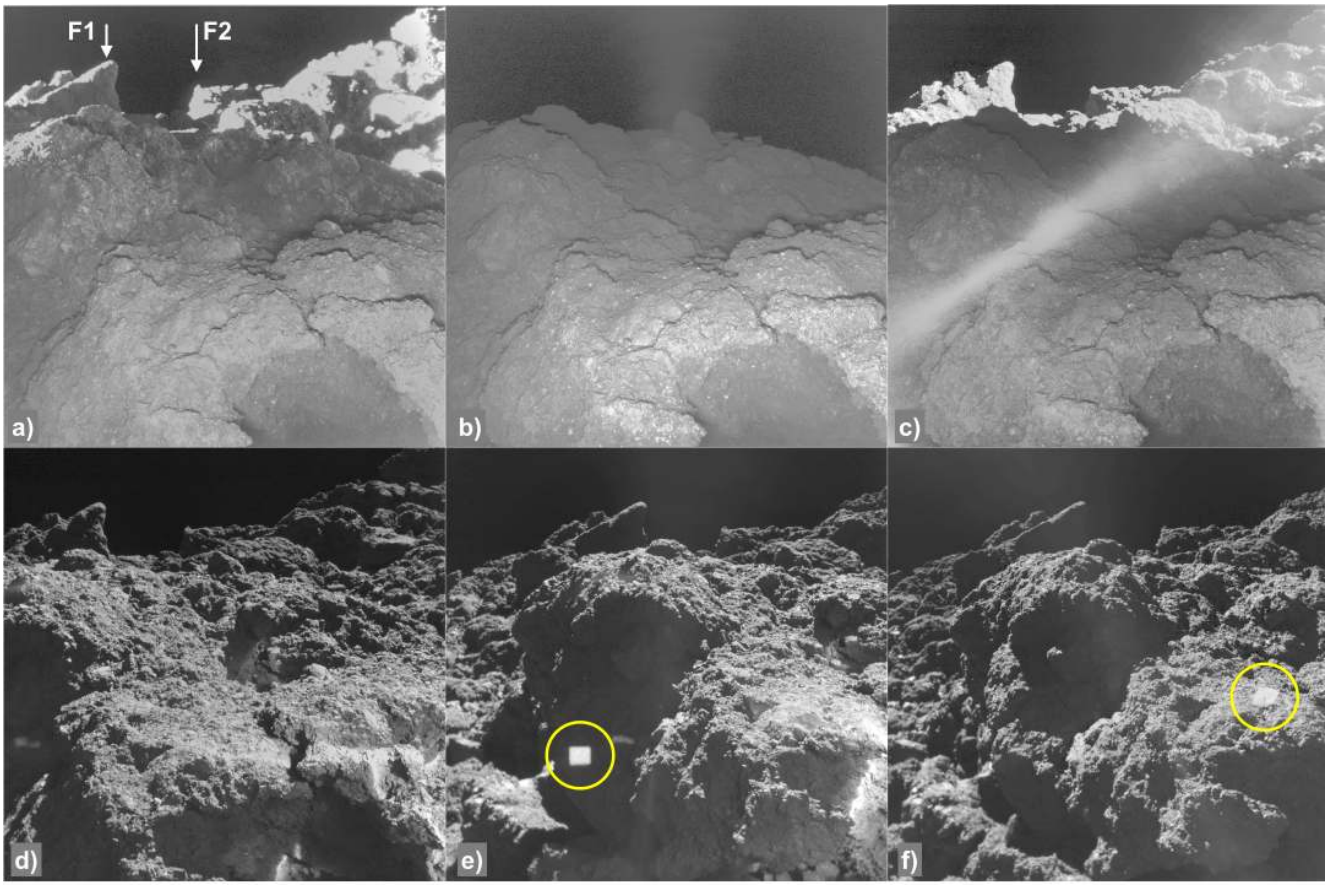

Fig. 2. Examples for MASCam images (red LED on, raw images stretched for display). *Top row*: (foreground in shadow): (*a*) sunset at MP2b (background features F1 and F2 are described in Sect. 3.2), (*b*) night at MP2c, and (*c*) morning at MP2c, with stray light. *Bottom row*: (daylight around local noon): (*d*) MP2a, (*e*) MP3a, and (*f*) MP3b. The reflections of the alignment cube at MP3a and MP3b are marked with yellow circles.

and one star within MASCam images during the first science sequence (Jaumann et al. 2019) and their celestial coordinates allowed us to determine the precise attitude of MASCOT at MP1a (see Table 3). Faint surface features in MP1b images indicate a change of MASCOT's orientation from MP1a to MP1b. However, these features are only visible at the edge of the images and cannot be related with certainty to features in other images; they do not allow a more quantitative description of the attitude at MP1b.

3.2. Measurement positions MP2 and MP3

In total, there are five different positions and attitudes of MASCOT during the two science cycles at MP2 and MP3. Stereophotogrammetric bundle block adjustment (Zhang et al. 1996) is the typical analysis tool for the precise determination of three-dimensional movements and attitude changes for such a set of images. The typical input is a set of image coordinates of identical points (tie-points). We selected and manually measured 21 tie-points in MASCam images of all five MPs. Together with camera calibration data, the least-squares adjustment process requires approximate values for the unknown camera orientation parameters (position and attitude). We derived such approximate values from the comparison of tie-point parallaxes in the foreground and in the background, since changes of the position and the attitude effect parallaxes depending on the distance. Initially, the absolute scale of the entire image scene and the relative displacements are also unknown. However, these can be constrained by two different sources: (1) from the known distance to identified background surface features F1 and F2 in 7.5 m and 9.2 m distance respectively (see Figs. 2a and 3a), measured in an ONC orthoimage (image ID 53167; see Preusker et al. 2019) and 2) from the reflection of the front side of an alignment cube, which is mounted on MASCOT right next to MASCam (Fig. 1). Sun reflections from this cube are visible in the foreground MASCam images at MP3a and MP3b (see Figs. 2e,f). From laboratory measurements during assembly of MASCOT, the position (Fig. 1) and the size (15 mm × 15 mm) of the front plane of this cube is precisely known. The well-calibrated IFOV (Instantaneous Field of View, about 1 mrad) of MASCam and the apparent size (in pixels) of these reflections in the images constrain the foreground distance and show that they appear at a distance from the MASCam entrance pupil of 33 cm at MP3a and 32 cm at MP3b. The uncertainty of the size of the reflections in the images is about 1 pixel. The respective uncertainty of the distances is about 1 cm. With this input, we performed the SPG bundle block adjustment and retrieved adjusted relative 3D displacements of MASCam's entrance pupil (accurate to ~0.1 mm) and 3D attitude changes (accurate to ~0.1°) at MP2 and MP3 relative to MP2a (see Table 2). With the eccentricity of MASCam in the MBFF (see Fig. 1) and with the known absolute position of the MBFF origin at MP3b in the RBFF (see Sects. 2.3 and 2.4), we derived absolute positions of the MBFF origin in the RBFF. Approximate values for the azimuths to north were retrieved from known azimuths to surface features in the background of some MASCam images (F1 and F2, see Figs. 2a and 3a).

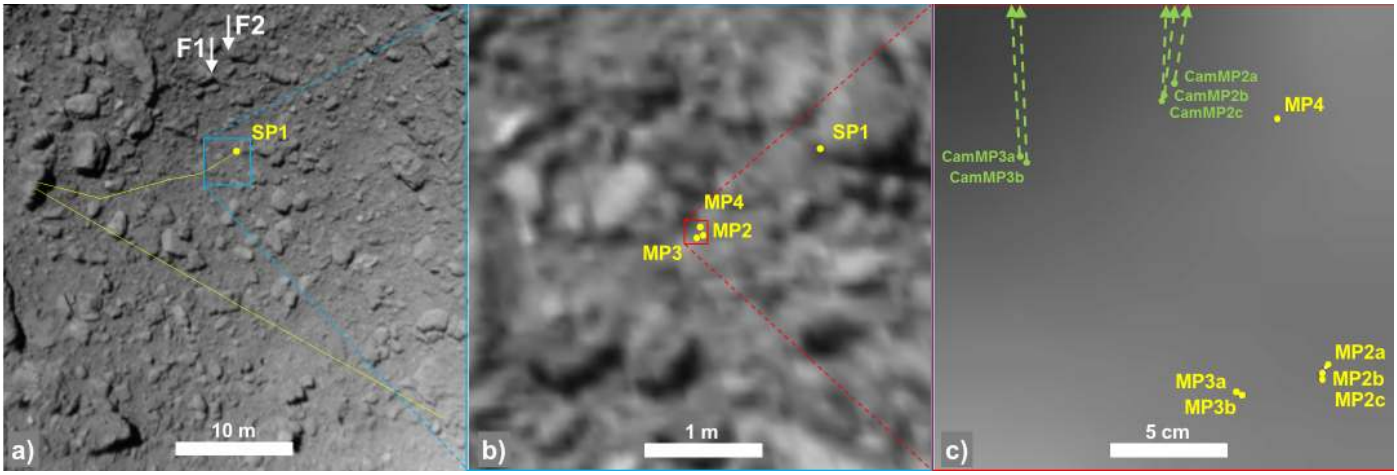

Fig. 3. Zoom sequence into an ONC orthoimage map (from Preusker et al. 2019). Positions of the MBFF origin (yellow). Respective positions of MASCam's entrance pupil and its viewing directions (green).

Table 2. Differences between MASCam positions at MP2 and MP3 in the MBFF (distances and rotations relative to MP2a).

Position	X [mm]	Y [mm]	Z [mm]	R_x [°]	R_y [°]	R_z [°]
2a	0.0	0.0	0.0	0.0	0.0	0.0
2b	−2.6	−6.1	−1.3	0.3	−0.3	1.3
2c	−2.8	−10.1	−1.0	0.4	−0.6	2.9
3a	−44.2	−31.6	−5.7	0.4	−2.2	12.1
3b	−42.0	−32.3	−4.5	0.4	−1.9	11.8

However, for the derivation of approximate values for the vertical tilt and yaw angles around the viewing direction, we used the apparent horizon. These approximations complete the preliminary absolute orientation of the entire set of the five MPs at MP2 and at MP3 in the RBFF (see Fig. 3).

3.3. Measurement position MP4

The position of MP4 is determined directly from ONC orthoimages (see Sect. 2.3), but the only MASCam image at MP4 indicates that MASCOT's orientation was upside-down. Thus, there is no possibility for a more quantitative reconstruction of MASCOT's orientation at MP4 from MASCam image data.

4. Thre-dimensional surface model of the vicinity of MASCOT and final orientations at all MPs

In the following, we report how we derived a full 3D description of the near and wider vicinity of the measurement positions. Section 4.1 is dedicated to the derivation of the local MASCam-based surface model and its refined orientation in the RBFF, while in Sect. 4.2 we describe the integration of this local model into the ONC-based context model. In Sect. 4.3, we finally summarize the results for MASCOT's orientation at all MPs.

4.1. Local MASCam-based surface model

The derivation of a 3D surface model of the near vicinity of MASCOT is limited by several aspects: (1) the surface must be visible in at least two images, (2) the respective images must provide a sufficient stereo base and convergence (stereo) angle, and (3) automated least-squares image matching (LSM) algorithms (Wewel 1996) require identical (or at least very similar) illumination within the stereo images. The previous results (see Table 2) show that the displacements between MP2 and MP3 positions only barely fulfill the typical conditions for stereo analysis, that is, significant stereo angles and baselengths. Therefore, the following 3D reconstruction of the surface of Ryugu at reasonable accuracy is limited to areas in the foreground (up to 0.4–0.5 m distance from MASCam). MASCam image combinations from MP2 and MP3 comprise the largest stereo angles and a side-overlap of about 70%, while images from MP2 subpositions provide smaller stereo angles, but almost 100% side-overlap. The different MASCam image series from MP2 and MP3 were acquired at different local times and, thus, under different illumination conditions. However, MASCam was operated with additional artificial illumination by LEDs, which are effective up to a distance of about 1 m. Thus, there are MP2 night images as well as MP2 day images (short after sunrise and short before sunset) that show the relevant parts of the images in the foreground in similar artificial illumination. Furthermore, the majority of scientific data of other MASCOT instruments (particularly from the MARA radiometer) result from measurements at MP2. The field-of-view of MARA mainly covers the right part of the MASCam field of view. Thus, only 50% is covered by the side-overlap of MP2 and MP3 images. Therefore, we selected only MASCam images from MP2b and MP2c with similar illumination by the LEDs as the stereo combination for the computation of a 3D surface model. We derived 850 000 mass tie-points from two stereo combinations using one MASCam image from MP2b as the master image and two different images from MP2c as stereo partners using LSM techniques. Using camera calibration data and the adjusted orientation data from SPG bundle block adjustment, we computed the coordinates of the tie-points by 3D forward-ray-intersection. The intersection accuracy was used for blunder elimination, which reduced the set of 3D coordinates to about 460 000 3D points. From these points, we derived a meshed dataset using the Poisson surface reconstruction functionality in the mesh processing system MeshLab©, version 1.3.3 (Cignoni et al. 2008). Additional blunder elimination and substantial noise reduction within this processing step (using MeshLab's Poisson Surface Reconstruction approach) reduced the final number of meshed points to about 7200 with a mean point spacing of about 5 mm. The

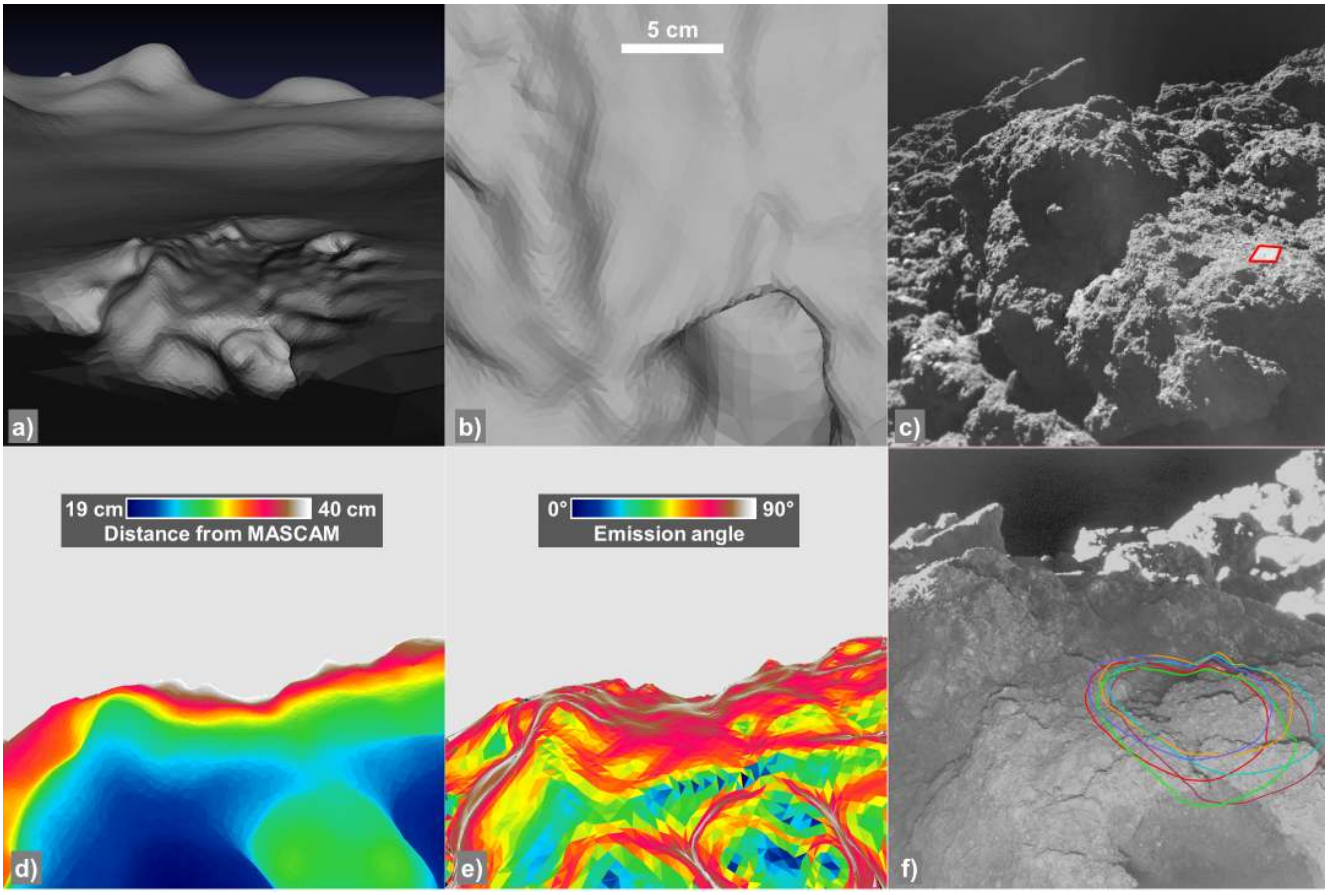

Fig. 4. Illustrations of the derived results. (*a*) 3D oblique view to the integrated shape model (local surface model in the foreground), (*b*) view from the top to local surface model, (*c*) nominal Sun reflection (marked in red) of the alignment cube on top of a raw MP3b image (MASCam image ID 850, comp. Fig. 2f), (*d,e,f*) derived datasets from the local surface model (up to 40 cm distance, for an exemplary MP2b raw image, see Fig. 2a), (*d*) distance layer, (*e*) emission angle layer, and (*f*) six MARA fields of view.

3D model covers an area of about 25 cm × 25 cm. Based on the initially derived absolute orientation (see Sect. 3.2) of all MASCam images from MP2 and MP3, we transformed the 3D model from MASCam image coordinate frame at MP2a to the RBFF. We then refined the initial orientation in the RBFF within brute-force-like simulations. These investigate how accurately the Sun reflections of the alignment cube hit the 3D surface model. The optimum solution corrected the approximate values of the three rotations azimuth, elevation, and yaw by 0.1°−2.3°. With this final orientation of the MASCam images in the RBFF, the observed reflections of the alignment cube perfectly match the nominal positions on the surface. The typical uncertainty within the 3D model depends on the accuracy of the applied LSM technique (~0.3 pixel), the actual stereo baselength (~3 mm), and the actual stereo angle, which decreases towards the background. Thus, the uncertainties of the DTM are about 0.5 cm in the foreground at a distance of 20 cm and about 1.5 cm at a distance of 30–40 cm.

4.2. Integration of the local MASCam-based surface model into the ONC-based surface model

The ONC-based landing site surface model (Preusker et al. 2019) describes the wider context around the local MASCam-based model. During the integration of the local model, the best-fit to the context model could be achieved with a final systematic correction of the radii by −0.12 m, which is within the uncertainty of the ONC context model. Figures 4a,b display the local MASCam-based surface model and the integrated surface model. Figure 4c proves the accuracy of the local surface model using the nominal reflection of the alignment cube. Figures 4d,e provide examples for derived datasets, for example image layers with distance information and illumination parameters per pixel. Finally, Fig. 4f shows the MARA field of view precisely related to MASCam image information.

4.3. Final RBFF positions and orientations of all MASCOT measurement points

With all previous calculations and the final radial correction of −0.12 m applied to MP1-4 (see Sect. 4.2), the final set of MASCOT positions and orientations in RBFF is complete and listed in Table 3. Here, rotations R follow the right-hand rule with (1) azimuth equal to R_z to local north (positive = the MBFF_+y axis is pointing northwestward), (2) elevation equal to R_x (positive = the MBFF_+y axis is pointing above the local spherical tangent), and (3) yaw equal to R_y (positive = the MBFF_−x axis is pointing above the local spherical tangent). The uncertainty of the parameters in absolute sense is about 10 cm for the positions and about 1° for the angles. Within the previous sections, we show that unintentional slides typically change MASCOT's attitude by only a few degrees and movements are as small as a few millimeters, and that the commanded mini-move to MP3 and the relocation to MP4 are also not larger than about 5–12 cm. Therefore,

Table 3. Final MASCOT positions (MBFF origin) in RBFF and orientations of the MBFF with respect to a local spherical tangential system (SP1 from Scholten et al. 2019).

Position	Latitude [°] South	Longitude [°] East	Radius [m]	Azimuth [°]	Elevation [°]	Yaw [°]
SP1	22.2065	317.2991	446.250	–	~−90.0	–
MP1a	22.305	317.158	446.24	74.7	5.7	171.5
MP1b	22.305	317.158	446.24	–	~0	~180.0
MP2a	22.3054	317.1578	446.041	−9.0	31.1	13.0
MP2b	22.3058	317.1574	446.037	−7.7	31.4	12.7
MP2c	22.3059	317.1576	446.036	−6.1	31.5	12.4
MP3a	22.3066	317.1526	446.030	3.1	31.5	10.8
MP3b	22.3068	317.1527	446.030	2.8	31.5	11.1
MP4	22.2940	317.1610	446.250	–	~180.0	–

Table 4. Effective movements of MASCOT on the surface of Ryugu.

Movement	Type	Horizontal [cm]	Vertical [cm]	Total 3D [cm]
SP1→MP1a	Uprighting	120–140	−5 to −10	120–140
MP1a→MP1b	Slide	0–1	~0	0–1
MP1b→MP2a	Relocation	0–10	~0	0–10
MP2a→MP2b	Slide	0.3	−0.4	0.5
MP2b→MP2c	Slide	0.2	−0.1	0.2
MP2c→MP3a	Mini-move	3.6	−0.6	3.7
MP3a→MP3b	Slide	0.2	0.0	0.2
MP3b→MP4	Relocation	11.6	1.0	11.7

we assume that the slide at MP1 is as small as the other slides and that during the relocation from MP1 to MP2 MASCOT simply lifted off, uprighted, and came to rest very close (within centimeters) to MP1. In addition, Table 4 shows a summary of the effective movements of MASCOT by the autonomous uprighting procedure from SP1 to MP1a, a slide to MP1b, the first commanded relocation to MP2a, the two unintentional slides to MP2b and MP2c, the commanded mini-move to MP3a, the unintentional slide to MP3b, and the final commanded relocation to MP4. Therein, effective movements are defined as real movements of the geometric center of the MASCOT structure (here, a simple flip of MASCOT from upside-down to the nominal orientation without changing the location is defined as a movement of zero). As for Table 3, the first three movements are uncertain because of the only weakly constrained positions MP1a and MP1b while the uncertainty in relative sense is at the millimeter level for the movements and less than 1° for the changes in attitude.

5. Summary and outlook

The intention of this investigation was to extend results from the analysis of the descent and bouncing phase of Hayabusa2's lander MASCOT. We provide precise geometric background information for any analysis of scientific data from MASCOT's instruments (particularly from MASCam and MARA) that have been acquired after MASCOT's settlement on the surface of Ryugu. Although the conditions for stereo-photogrammetric image processing were difficult, we investigated MASCam images and derived a complete set of 3D positions and orientations of MASCOT for the measurement points MP2 and MP3 where MASCOT was in an upright orientation. Based on context information from ONC image data, the results are precisely referenced in the Ryugu body-fixed frame. Thus, they can be directly combined with external information, such as the position of the Sun for example. MASCOT's orientation at MP1 and MP4 was obviously upside-down. While we derived MASCOT's attitude at MP1a from the visibility of Jupiter and Saturn, quantitative information about the complete orientation at MP1 and MP4 cannot be derived from MASCam image data. Nevertheless, the positions of MP1 (with some uncertainty, not constrained by ONC images) and of MP4 have been determined. The calculated changes of the position will support the analysis of the performance of MASCOT's mobility mechanism. Finally, we derived a high-resolution 3D surface model of a part of MASCOT's vicinity. With this central data product it is possible to precisely relate measurements from the MARA radiometer (with only a few millimeters uncertainty) to the surface and to retrieve the surface inclination to the Sun over MARA's entire field of view. Furthermore, this information allows precise quantitative measurements for surface features that are visible in MASCam images at submillimeter to millimeter scales. The results and data products of this investigation, that is, SPICE kernels of the derived surface models and of MASCOT's position and attitude, are available at the Europlanet website[1].

Acknowledgements. The Hayabusa2 mission is operated by JAXA. The MASCOT lander on the Hayabusa2 mission is a DLR/CNES cooperation. This work was partially supported by JSPS KAKENHI 17KK0097. The authors acknowledge funding by JAXA, CNES, and DLR. as well as the work of the different instrument teams of Hayabusa2 and MASCOT that made the different instrument measurements possible. We thank Katharina Otto and Volker Mertens (DLR) for their support during the review and submission process.

References

Acton, C. H. 1996, Planet. Space Sci., 44, 65
Cignoni, P., Callieri, M., Corsini, M., et al. 2008, in Eurographics Italian Chapter Conference 2008, Salerno, Italy, 129
Grott, M., Knollenberg, J., Borgs, B., et al. 2016, Space Sci. Rev., 208, 413
Grott, M., Knollenberg, J., Hamm, M., et al. 2019, Nat. Astron., 406
Gwinner, K., Scholten, F., Spiegel, M., et al. 2009, Photogramm. Eng. Remote Sens., 75, 1127
Gwinner, K., Scholten, F., Preusker, F., et al. 2010, Earth Planet. Sci. Lett., 294, 506
Ho, T.-M., Baturkin, V., Grimm, C., et al. 2017, Space Sci. Rev., 208, 339
Jaumann, R., Schmitz, N., Koncz, A., et al. 2017, Space Sci. Rev., 208, 375
Jaumann, R., Schmitz, N., Ho, T.-M., et al. 2019, Science, 365, 817
Kameda, S., Suzuki, H., Takamatsu, T., et al. 2017, Space Sci. Rev., 208, 17
Preusker, F., Oberst, J., Head, J. W., et al. 2011, Planet. Space Sci., 59, 1910
Preusker, F., Scholten, F., Knollenberg, J., et al. 2012, Planet. Space Sci., 66, 54
Preusker, F., Scholten, F., Matz, K.-D., et al. 2017, A&A, 607, L1
Preusker, F., Scholten, F., Elgner, S., et al. 2019, A&A, 632, L4
Scholten, F., Oberst, J., Matz, K.-D., et al. 2012, J. Geophys. Res., e00117, H17
Scholten, F., Preusker, F., Elgner, S., et al. 2019, A&A, 632, L3
Sugita, S., Honda, R., Morota, T., et al. 2019, Science, 364
Watanabe, S., Tsuda, Y., Yoshikawa, M., et al. 2017, Space Sci. Rev., 208, 3
Watanabe, S., Hirabayashi, M., Hirata, N., et al. 2019, Science, 364, 268
Wewel, F. 1996, Int. Arch. Photogram. Remote Sens., 31, 936
Zhang, W., Giese, B., Oberst, J., & Jaumann, R. 1996, Int. Arch. Photogram. Remote Sens., 31, 1004

[1] http://europlanet.dlr.de/MASCOT